

05,12

## Synthesis and magnetic properties of zinc-tellurite glasses activated by magnetite nanoparticles

© M.V. Shestakov<sup>1</sup>, I.I. Makoed<sup>2,\*</sup>, V.V. Moshchalkov<sup>3</sup>

<sup>1</sup> Russian State Agrarian University — Moscow Timiryazev Agricultural Academy, Moscow, Russia

<sup>2</sup> Brest State A.S. Pushkin University, Brest, Belarus

<sup>3</sup> Katholieke Universiteit Leuven, Leuven, Belgium

\* E-mail: igmak2010@yandex.by

Received March 16, 2023

Revised March 16, 2023

Accepted March 17, 2023

An effect of activation with nanosized particles  $\text{Fe}_3\text{O}_4$  on structural and magnetic properties of zinc-tellurite glasses  $20 \cdot \text{ZnO} - (80-x) \cdot \text{TeO}_2 - x \cdot \text{Fe}_3\text{O}_4$  ( $x = 0, 1, 3, 7$ ), prepared with melt-quenching method, have been investigated. Some functional properties of the glasses were experimentally investigated with X-ray diffraction, Energy dispersive and Raman spectroscopies, and SQUID magnetometry. The values of the average crystallite sizes calculated with Scherer and Williamson–Hall methods were comparable with the sizes of magnetically active clusters reconstructed from the results of processing of the magnetic field dependences of the values of specific magnetizations, indicating their effect on the change in the magnetic properties of activated glasses. A partial phase transformation, caused by oxidation of  $\text{Fe}^{2+}$  into  $\text{Fe}^{3+}$  ions, of ferrimagnetic magnetite  $\text{Fe}_3\text{O}_4$  into paramagnetic maghemite  $\gamma\text{-Fe}_2\text{O}_3$  has been revealed.

**Keywords:** glass, glass-ceramics, nanoparticle, magnetite, magnetism.

DOI: 10.21883/PSS.2023.05.56049.36

### 1. Introduction

Glasses and glass-ceramics synthesized on the basis of double  $\text{TeO}_2-\text{ZnO}$  system are distinguished by good solubility of various oxides, relatively low melting temperature and high glass-forming capability. Such materials are perspective as hosts for synthesis of new functional materials with pre-defined physical properties. Preparation of glasses from nominally pure  $\text{TeO}_2$  is hindered by high devitrification probability upon melt cooling [1]. Therefore, various modifiers are often added to  $\text{TeO}_2$  for glass synthesis. For this purpose,  $\text{ZnO}$  is often used [2,3]. Simultaneous addition of several various oxides into double  $\text{TeO}_2-\text{ZnO}$  system is a perspective method for modification of physical property of glasses [4,5].

Glass activation by various iron oxides is generally performed in order to produce multiferroics [6–8] or spin glasses [9].  $\text{Fe}_3\text{O}_4$  magnetite is considered as one of the most perspective materials for use as a zinc-tellurite glass activator due to its intrinsic chemical stability and high specific magnetization and permeability [10]. Synthesis and investigations of physical properties of magnetite-activated glasses and glass-ceramics is of interest in order to identify the preparation conditions and determine the optimal concentrations of doping particles. Despite of the extensive research in the field of new magnetic materials being synthesized on the basis of glasses, a relatively little

number of articles, describing the preparation conditions and study of such kind of compounds, is known [7,11–14].

The purpose of this study is to investigate the effect of activation with nanoscale magnetic particles on physical properties of  $20 \cdot \text{ZnO} - (80-x) \cdot \text{TeO}_2 - x \cdot \text{Fe}_3\text{O}_4$  ( $x = 0, 1, 3, 7$ ) glasses and glass-ceramics.

### 2. Experiment procedure

Nominally pure zinc-tellurite glasses and activated with nanoscale magnetite particles were prepared by melt quenching method. In order to avoid the evaporation of melt components, the crucible was covered with a lid and placed into a vertically-loaded muffle furnace preheated to  $850^\circ\text{C}$ . Glass batch compositions may be described by a general formula  $20 \cdot \text{ZnO} - (80-x) \cdot \text{TeO}_2 - x \cdot \text{Fe}_3\text{O}_4$ , where  $x = 0, 1, 3, 7$  mole%. Stoichiometric batch was carefully mixed in a mortar and placed in an alumina crucible. In order to avoid the evaporation of melt components, the crucible was covered with a lid and placed into a vertically-loaded muffle furnace preheated to  $850^\circ\text{C}$ . After holding at the specified temperature for 20 min, the crucible was removed from the furnace and the melt was poured down into an aluminum mold at room temperature. Glass-ceramics was obtained after cooling down the melt in the aluminum mold to  $400^\circ\text{C}$  followed with the heat-treatment at  $400^\circ\text{C}$  for 1 hour.

Diffraction patterns ( $2\theta$  angle range — from 10 to  $60^\circ$ , increment  $0.025^\circ$ ) were obtained using PANalytical X'Pert Pro X-ray diffractometer with  $\text{Cu } K_\alpha$  ( $\lambda = 1.5418 \text{ \AA}$ ) radiation. Full-profile analysis of diffraction patterns by the Rietveld method was carried out using JANA2020 software [15]. Glass-ceramics sample structure was analyzed using diffraction patterns recorded at room temperature on DRON 3M diffractometer in the  $2\theta$  range from  $5^\circ$  to  $100^\circ$  with increment  $0.04^\circ$  using  $\text{Cu } K_\alpha$  ( $\lambda = 1.5418 \text{ \AA}$ ) radiation. Energy-dispersive X-ray fluorescence analysis was carried out using Oxford-Instruments INCA 400 with X-Max detector. Raman scattering spectra were measured using a spectral analytical system based on Nanofinder (SP „LOTIS TII“, Republic of Belarus) confocal scanning microscope with 600 grooves/mm diffraction grating. The spectra were recorded using  $100\times$  optical lens for 30 s with 473 nm  $800 \mu\text{W}$  laser. Magnetic field dependences of specific magnetizations of samples were measured using Quantum Design MPMSXL-5 instrument at room temperature and 5 K.

### 3. Results and Discussion

Magnetite is an oxide with inverted spinel structure containing aliovalent  $\text{Fe}^{3+}$  and  $\text{Fe}^{2+}$  cations. Inversion is based on the fact that the cations  $\text{Fe}^{3+}$  occupy tetrahedral and a half of octahedral positions formed by oxygen anions, and  $\text{Fe}^{2+}$  occupy a half of octahedral positions. Formula written as  $(\text{Fe}^{3+})_{\text{tetra}}[\text{Fe}^{2+}\text{Fe}^{3+}]_{\text{octa}}\text{O}_4$  reflects cation distribution and magnetic structure shown in Figure 1.

Amorphous glass structure is confirmed by the presence of a wide reflection with diffused maximum near  $2\theta = 28^\circ$  and the absence of any narrow reflections specific to crystalline phases. The glass-ceramics diffraction pattern, corresponding to nominally pure (undoped) zinc-tellurite glass, shows a set of narrow sharp peaks assigned to  $\text{Fe}_2\text{O}_3$  phase besides the X-ray signal from the amorphous phase. No lines associated with the magnetite phase were detected. This is explained by the fact that the samples are synthesized in liquid medium at relatively high temperature. When magnetite is heated to temperatures above  $300^\circ\text{C}$ , its thermal decomposition occurs with formation of a set of iron oxides [16–18]. The best known oxides, which appearance is possible depending on the preparation conditions, include  $\alpha\text{-Fe}_2\text{O}_3$  (space group  $R\bar{3}\bar{c}$  with  $a = 5.034 \text{ \AA}$  and  $c = 13.752 \text{ \AA}$ ),  $\beta\text{-Fe}_2\text{O}_3$  ( $I\bar{a}\bar{3}$  from  $a = 9.393 \text{ \AA}$ ),  $\gamma\text{-Fe}_2\text{O}_3$  ( $Fd\bar{3}m$  from  $a = 8.351 \text{ \AA}$ ),  $\epsilon\text{-Fe}_2\text{O}_3$  ( $Pna_1$  from  $a = 5.072 \text{ \AA}$ ,  $b = 8.736 \text{ \AA}$  and  $c = 9.418 \text{ \AA}$ ) [17,18]. These phases are difficult to identify in the experimental diffraction pattern, as the diffraction angles corresponding to them are close to each other and the intensity of line is low.

The diffraction pattern analysis shows that neither the listed phases nor the initial magnetite may be correlated with the experimental data. During synthesis of glass activated by magnetite particles, iron oxide clusters are formed as a result of oxidation and iron atom diffusion.

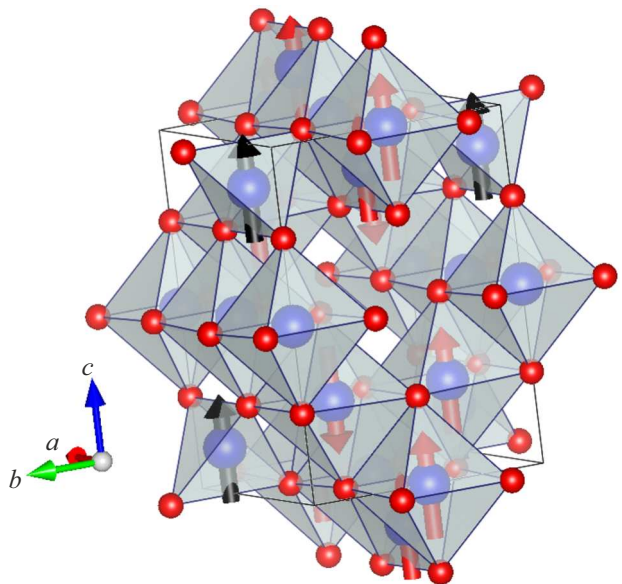


**Figure 1.** A part of crystalline and magnetic structure of magnetite.

Depending on the synthesis temperature and time, various phases may be formed and co-exist. nanoscale  $\gamma\text{-Fe}_2\text{O}_3$  particles are often described in the archetypic space group of  $Fd\bar{3}m$  spinel. This hampers reliable distinguishing of magnetite and maghemite structures with various vacancy ordering. Unlike  $\text{Fe}_3\text{O}_4$  containing both  $\text{Fe}^{3+}$  and  $\text{Fe}^{2+}$ , all iron cations in  $\gamma\text{-Fe}_2\text{O}_3$  are in trivalent state. Charge neutrality in  $\gamma\text{-Fe}_2\text{O}_3$  spinel structure is maintained by introduction of vacancies ( $\Delta$ ) into octahedrally coordinated cation positions. According to the findings in [19],  $\gamma\text{-Fe}_2\text{O}_3$  configuration with space group  $P4_12_12$  is the most stable comparing to other possible structures, as it is represented by the highest distribution uniformity of iron cations and vacancies. Therefore, modifications of  $\gamma\text{-Fe}_2\text{O}_3$  maghemite with the following crystal-chemical formulas were studied as the most probable ones [20]: 1)  $(\text{Fe}^{3+})[\text{Fe}_{5/3}^{3+}\Delta_{1/3}] (\text{O}^{2-})$  (Space group  $FD\bar{3}m$  (227), Lattice parameters  $a = b = c = 8.3540 \text{ \AA}$ ,  $\alpha = \beta = \gamma = 90^\circ$ , JCPDS card 04-013-7114); 2)  $(\text{Fe}_8^{3+})[\text{Fe}_{4/3}^{3+}\Delta_{8/3}\text{Fe}_{12}^{3+}] (\text{O}^{2-})_{32}$  ( $P4_332$  (212),  $a = b = 8.3296 \text{ \AA}$ ,  $c = 8.3221 \text{ \AA}$ ,  $\alpha = \beta = \gamma = 90^\circ$ , JCPDS card 04-016-4344); 3)  $(\text{Fe}_{24}^{3+}[\text{Fe}_{40}^{3+}\Delta_8] (\text{O}^{2-})_{96}$  ( $P4_12_12$  (92),  $a = b = 8.3470 \text{ \AA}$ ,  $c = 25.0100 \text{ \AA}$ ,  $\alpha = \beta = \gamma = 90^\circ$ , JCPDS card 04-007-2135).

The results shown in Figure 2 illustrate the difficulty in identification of different phases in the studied glass-ceramic samples. Table 1 shows the diffraction pattern processing results by the Rietveld method taking into account the possible presence and co-existence of different phases.

Diffraction peaks of the tetragonal maghemite with totally-ordered vacancy distribution (space group  $P4_12_12$ ) confirm the partial phase transformation of magnetite into maghemite as a result of oxidation and diffusion processes. Medium degree of iron oxidation, degree of vacancy

**Table 1.** Crystal lattice constants ( $a$ ,  $b$ ,  $c$ ,  $\alpha$ ,  $\beta$ ,  $\gamma$ ) refined by the Rietveld method and fitting criteria of (GOF,  $R_p$ ,  $wR_p$ )  $Zn_2Te_3O_8$  and  $\gamma\text{-Fe}_2O_3$  glass-ceramics phases

Material	Space group (№)	Lattice constants						Fitting parameters
		$a$ , Å	$b$ , Å	$c$ , Å	$\alpha$	$\beta$	$\gamma$	
$Zn_2Te_3O_8$	C2/c (15)	12.7100	5.2100	11.820	90	100	90	GOF = 0.19 $R_p$ = 3.05 $wR_p$ = 10.11
$\gamma\text{-Fe}_2O_3$	P4 <sub>3</sub> 32 (212)	8.3457	8.3457	8.3457	90	90	90	GOF = 0.37 $R_p$ = 7.13 $wR_p$ = 20.59
$\gamma\text{-Fe}_2O_3$	P4 <sub>1</sub> 2 <sub>1</sub> 2 (92)	8.5604	8.5604	25.9039	90	90	90	GOF = 0.46 $R_p$ = 6.35 $wR_p$ = 9.60

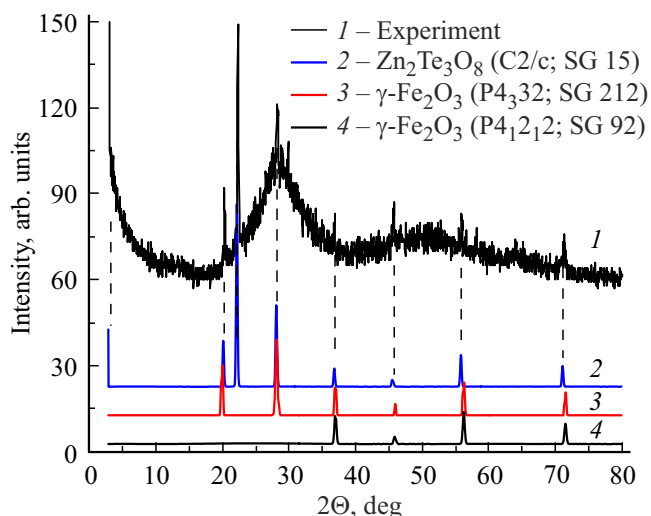


**Figure 2.** Experimental diffraction pattern of  $20 \cdot ZnO - 79 \cdot TeO_2 - 1 \cdot Fe_3O_4$  glass-ceramics sample and calculated diffraction patterns of  $Zn_2Te_3O_8$  and two  $\gamma\text{-Fe}_2O_3$  modifications.

ordering and magnetic properties depend on the preparation method, reaction conditions and nanoparticle sizes. To investigate the structure and estimate the average crystallite size by Scherrer and Williamson–Hall methods, a glass-ceramics diffraction pattern, depicted in Figure 3, was used, *a*.

Average crystallite size  $D_S$  of the synthesized glass-ceramics was calculated by X-ray line broadening method using the Scherrer equation [21]:

$$D_S = \frac{K \cdot \lambda}{\beta \cdot \cos \theta}, \quad (1)$$

where  $K = 0.89$  is the Scherrer constant associated with the crystallite shape;  $\lambda$  is X-ray wavelength  $Cu K_\alpha$  (0.15418 nm);  $\beta$  is the integral peak width;  $\theta$  the Bragg angle in radians.

Taking into account that the integral peak width on the diffraction pattern is approximated by the pseudo-Voigt function with major (up to 90% or higher) contribution of the Lorentz function, the Lorentzian was used to describe the diffraction reflection form at  $2\theta \approx 22.34^\circ$ .

Crystallite size ( $D_{WH}$ ) and broadening of Bragg peak diffraction induced by lattice micro deformation ( $\varepsilon$ ) in glass-ceramics were calculated using the Williamson–Hall method [22]:

$$\beta_{hkl} \cdot \cos \theta_{hkl} = \frac{K \cdot \lambda}{D_{WH}} + 4\varepsilon \cdot \sin \theta_{hkl}, \quad (2)$$

here, structural constants  $K$ ,  $\lambda$  and  $\beta_{hkl}$  have the same meaning as in the Scherrer equation (1),  $D_{WH}$  is the crystallite grain size. For  $20 \cdot ZnO - 79 \cdot TeO_2 - 1 \cdot Fe_3O_4$  glass-ceramics sample, crystallite size  $D_{WH}$  established from the Williamson–Hall curve (Figure 3, *b*) is equal to 47.65 nm, which correlates well with the assessment using the Scherrer equation ( $D_S \sim 50$  nm). Stresses also contribute to diffraction peak line broadening, and the absolute value of  $\varepsilon$  obtained on the basis of analysis of the Williamson–Hall curve is positive and equal to 0.0028. These parameters shall influence the structurally sensitive magnetic properties of samples.

For the purpose of sample structure and composition qualification, energy-dispersive analysis was carried out and Raman scattering spectra at room temperature were recorded, see Figure 4, *a*. The energy-dispersive analysis of glass-ceramics is shown in Figure 4, *b* and supports the chemical purity of  $20 \cdot ZnO - 79 \cdot TeO_2 - 1 \cdot Fe_3O_4$  sample. Vertical arrows indicate the signal from the substrate material. The spectrum contains characteristic peaks assigned to Te, Zn, Fe and O. Weight % of the elements are listed in the Table in the Detail of Figure 4, *b*.

Wide bands specific to zinc-tellurite glasses are observed in the spectra. A wide band with its maximum in the range from 400 to  $500 \text{ cm}^{-1}$  is associated with tension and compression of Te–O–Te bridge bonds in  $TeO_4$ ,  $TeO_3$ ,

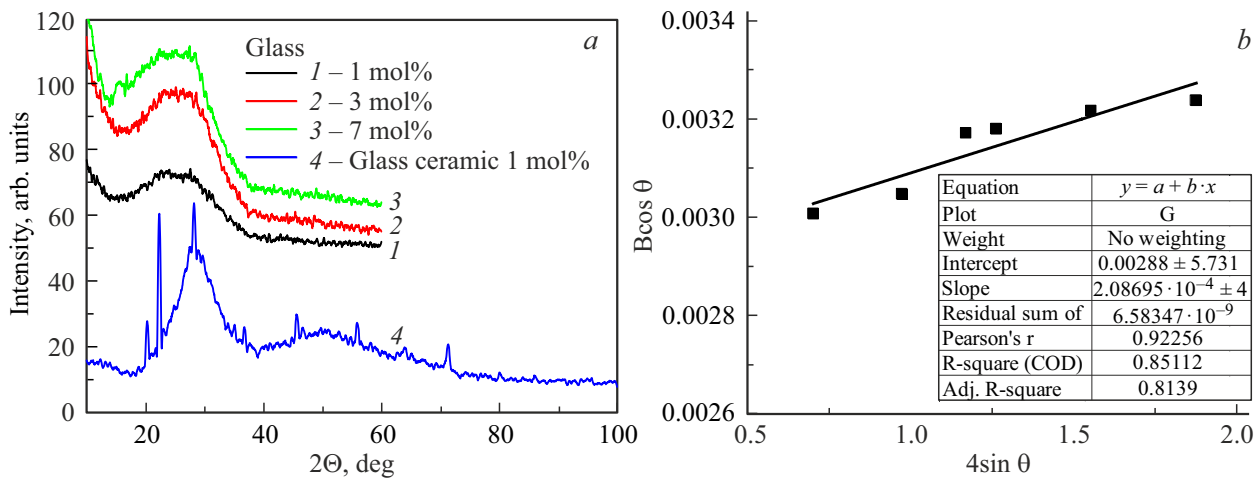


**Figure 3.**  $20 \cdot \text{ZnO} - (80-x) \cdot \text{TeO}_2 - x \cdot \text{Fe}_3\text{O}_4$  ( $x = 0, 1, 3, 7$ ) glass and  $20 \cdot \text{ZnO} - 79 \cdot \text{TeO}_2 - 1 \cdot \text{Fe}_3\text{O}_4$  glass-ceramics diffraction patterns (a). Williamson–Hall curve for  $20 \cdot \text{ZnO} - 79 \cdot \text{TeO}_2 - 1 \cdot \text{Fe}_3\text{O}_4$  glass-ceramics sample (b).

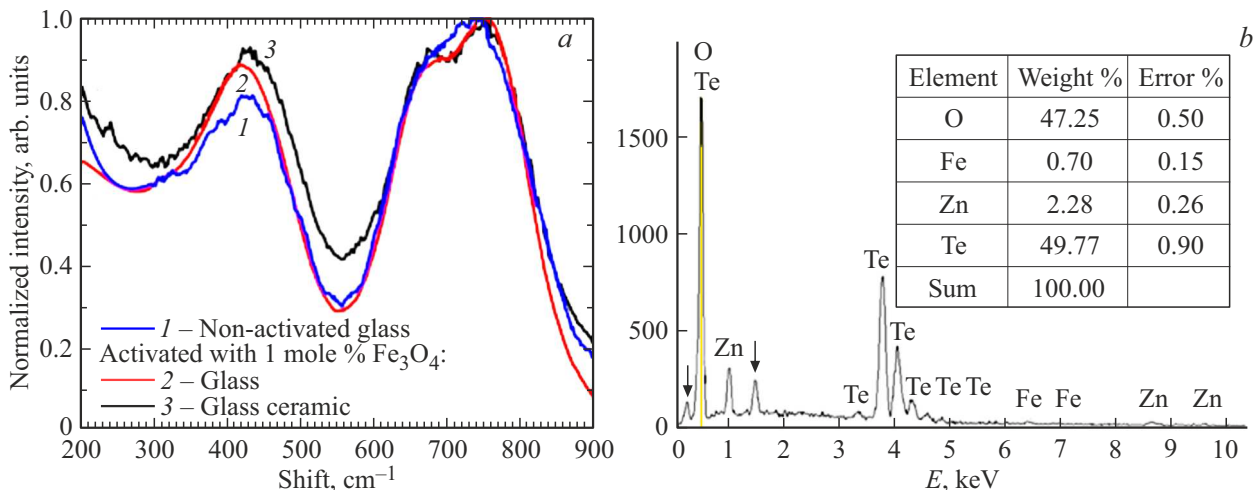


**Figure 4.** Raman scattering spectra (a) of  $20 \cdot \text{ZnO} - 80 \cdot \text{TeO}_2$  and  $20 \cdot \text{ZnO} - 79 \cdot \text{TeO}_2 - 1 \cdot \text{Fe}_3\text{O}_4$  glasses and  $20 \cdot \text{ZnO} - 79 \cdot \text{TeO}_2 - 1 \cdot \text{Fe}_3\text{O}_4$  glass-ceramics. Energy-dispersive analysis data (b) of  $20 \cdot \text{ZnO} - 79 \cdot \text{TeO}_2 - 1 \cdot \text{Fe}_3\text{O}_4$  glass-ceramics sample.

$\text{TeO}_{3+\delta}$  structural systems. Two wide Raman scattering bands located between 600 and 900 cm<sup>-1</sup> are caused by vibrations of the lattice composed of trigonal  $\text{TeO}_4$  bipyramids, antisymmetric vibrations of  $\text{Te}-\text{O}-\text{Te}$  bonds and tension of  $\text{Te}-\text{O}$  non-bridge bonds [23]. When glasses are activated by iron oxide, relative growth of wide band intensity with maximum near 420–430 cm<sup>-1</sup> was detected, which is indicative of iron oxide dissolution in the glass followed by failure of  $\text{Te}-\text{O}-\text{Te}$  bridge bonds [23].

Magnetic field dependences of specific magnetizations as shown in Figure 5, a, b support the occurrence of magnetic phases in the studied materials as a result of  $20 \cdot \text{ZnO} - 80 \cdot \text{TeO}_2$  glass activation.

As can be seen, glass non-activated by iron oxide is diamagnetic. Dependences  $M(B)$  of magnetite-activated glasses at room temperature are almost linear and reflect

paramagnetic behavior of sample material. The presence of a low coercive field at room temperature indicates that particles do not act as supermagnetic. At low (5K) temperatures, magnetic field dependences are S-shaped with open hysteresis loops typical of ferromagnetic materials with low coercive fields and residual specific magnetization. In magnetic fields up to 2 T, no magnetization saturation occurs. For magnetic particle size assessment, hysteresis loop simulation was carried out for the samples using expression [24]:

$$M = M_s \frac{2}{\pi} \operatorname{arctg} \left( \frac{B \pm B_c}{B_T} \right), \quad (3)$$

where  $\mathbf{B}_c = \mathbf{H}_c \cdot \mu_0$  is the coercive field strength,  $B_T$  is the anisotropy threshold field above which magnetization is uniform. Specific saturation magnetization  $M_s$

**Table 2.** Specific residual magnetizations ( $M_r$ ), specific saturation magnetizations ( $M_s$ ), coercive field strengths ( $B_c$ ), magnetic moments ( $\mu$ ) and nanoparticle sizes ( $D$ ) of  $20 \cdot \text{ZnO} - (80-x) \cdot \text{TeO}_2 - x \cdot \text{Fe}_3\text{O}_4$  ( $x = 0; 1; 3; 7$ ) glass samples

Composition (mol%)	5 K				300 K				$D$ (nm)
	$M_r$ (emu/g)	$B_c$ (T)	$M_s$ (emu/g)	$\mu$ ( $\mu_B$ )	$M_r$ (emu/g)	$B_c$ (T)	$M_s$ (emu/g)	$\mu$ ( $\mu_B$ )	
1	0.00099	0.00900	3.700	8.60	0.0000012	0.00100	0.120	0.28	34.6
3	0.00160	0.00098	5.700	9.03	0.000068	0.0013	0.350	0.53	29.9
7	0.00175	0.00082	6.100	8.92	0.00014	0.0096	0.650	0.92	29.3

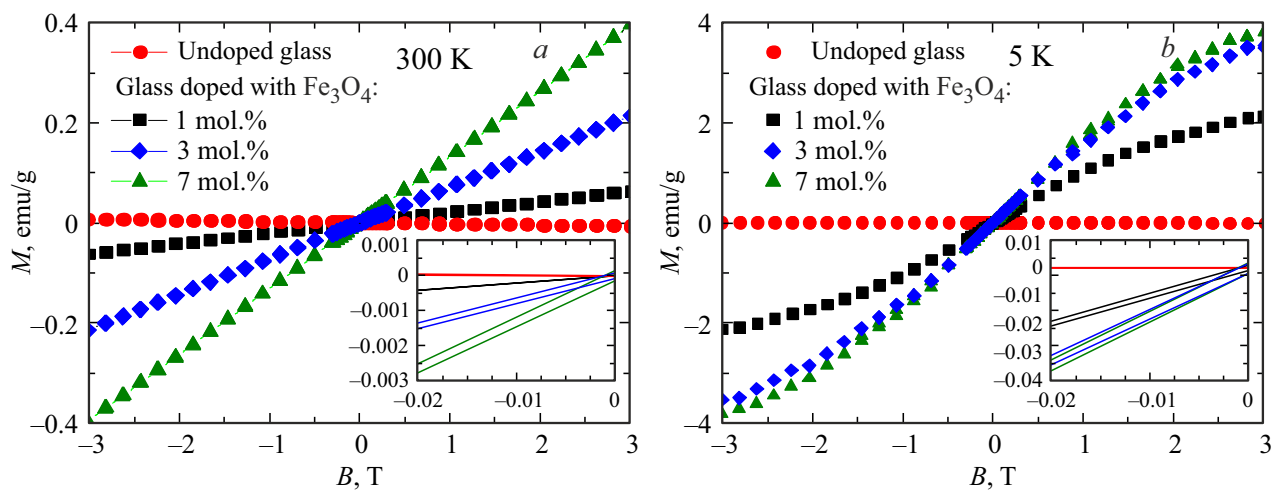


**Figure 5.** Magnetic field dependences of specific magnetizations of  $20 \cdot \text{ZnO} - 80 \cdot \text{TeO}_2$  (circles),  $20 \cdot \text{ZnO} - 79 \cdot \text{TeO}_2 - 1 \cdot \text{Fe}_3\text{O}_4$  (squares),  $20 \cdot \text{ZnO} - 77 \cdot \text{TeO}_2 - 3 \cdot \text{Fe}_3\text{O}_4$  (rhombs) and  $20 \cdot \text{ZnO} - 73 \cdot \text{TeO}_2 - 7 \cdot \text{Fe}_3\text{O}_4$  (triangles) glasses measured at (a) 300 K and (b) 5 K.

was varied so that to achieve the best match of the simulated and experimental curves. Curve simulation of  $20 \cdot \text{ZnO} - 79 \cdot \text{TeO}_2 - 1 \cdot \text{Fe}_3\text{O}_4$  glass samples is shown in Figure 6. Particle sizes  $D$  reestablished from this curve are comparable by the absolute value with the data obtained using the Scherrer equation. Correlation of specific saturation magnetization with the activator nanoparticle concentration, i.e. reduction of  $M_s$  with growth of particle sizes in magnetic regions is indicative of their impact on the magnetic properties of the magnetite-activated glasses.

Hysteresis loop parameters of glass samples at 5 K and 300 K and reestablished magnetic moments ( $\mu$ ) and nanoparticle sizes ( $D$ ) of samples are listed in Table 2.

With growth of activator concentration, residual magnetization ( $M_r$ ) grows, while coercive field ( $B_c$ ) decreases at low temperatures and increases at high temperatures. This is associated with reduction of magnetic cluster sizes when the amount of iron oxides in the samples grows. Behavior of  $M_s$  of the activated samples keeps to the same trend, and  $M_s$  decreases on a regular basis with increase in the non-magnetic phase content. Lower content of magnetic phase which is embedded in the amorphous diamagnetic matrix during synthesis shall not facilitate an increase in magnetoactive cluster sizes, while the large

fraction of iron oxides serve to promote clusterization processes and growth of magnetic region sizes. However, due to low activator concentrations, presence of strong

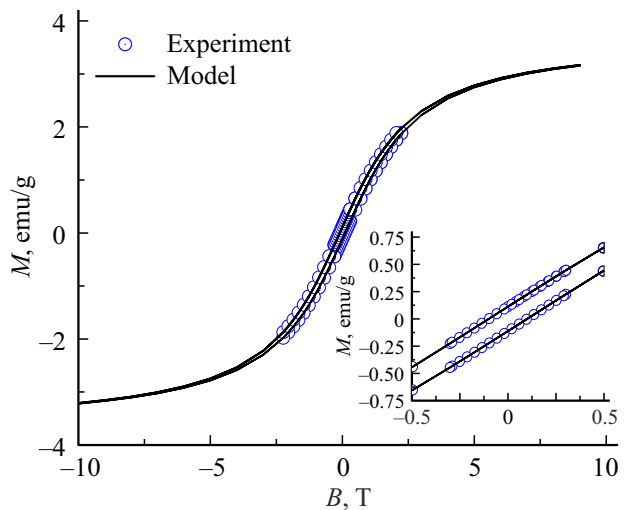


**Figure 6.** Experimental (dots) and calculated (line) by equation (3) hysteresis loops of  $20 \cdot \text{ZnO} - 79 \cdot \text{TeO}_2 - 1 \cdot \text{Fe}_3\text{O}_4$  glass-ceramics sample at 5 K.

magnetic interactions between them that influence the diffusion processes, these nucleation mechanisms affect the magnetic cluster formation conditions to a lesser extent than it could have been expected in case of glass activation with low-magnetic nanoparticles. During sample annealing, coalescence processes are activated and small crystallite group together forming larger clusters. The presence of magnetoactive clusters is supported by the shape of the open hysteresis loops observed in the low magnetic field region.

#### 4. Conclusion

A melt-quenching method was used to synthesize tellurite glasses and glass-ceramics activated with nanoscale magnetite particles. X-ray diffraction investigations confirm the amorphous state of glasses and occurrence of a crystalline phase in the form of  $\gamma\text{-Fe}_2\text{O}_3$  in the glass-ceramics. The magnetic property investigations prove that maghemite clusters are formed during synthesis and ensure the Raman response intensity enhancement and occurrence of a weak ferromagnetic response.

#### Funding

The authors are grateful to the government of Flanders (Belgium) and Post Doctoral Mandate PDM/16/108 (KU Leuven internal funds) for the financial support of the research (Methusalem grant) and V. Lozenko (ASML, Netherlands) for assistance in measurements.

#### Conflict of interest

The authors declare that they have no conflict of interest.

#### References

- [1] J. Majzlan, S. Notz, P. Haase, E.I. Kamitsos, N.S. Tagiara, E. Dachs. *Geochemistry* **82**, 125915 (2022).
- [2] H.J.L. Clabel, G. Lozano, E. Marega, V.A.G. Rivera. *J. Non-Cryst. Solids* **553**, 120520 (2021)
- [3] O.A. Zamyatin, M.F. Chubanov, E.V. Zamyatina. *Neorgan. materialy* **55**, 750 (2019). (in Russian).
- [4] I.V. García-Amaya, M.E. Zayas, J. Alvarado-Rivera, M. Cortez-Valadez, M. Pérez-Tello, N. Cayetano-Castro, F. Martínez-Suárez, A. Mendoza-Córdova. *J. Non-Cryst. Solids* **499**, 49 (2018).
- [5] J. de Clermont-Gallerande, D. Taniguchi, M. Colas, P. Thomas, T. Hayakawa. *Phys. Status Solidi B* **259**, 2200065 (2022).
- [6] R.P. Maiti, S. Basu, S. Bhattacharya, D. Chakravorty. *J. Non-Cryst Solids* **355**, 2254 (2009).
- [7] W. Widanarto, M.R. Sahar, S.K. Ghoshal, R. Arifin, M.S. Rohani, M. Effendi. *Mater. Lett.* **108**, 289 (2013).
- [8] A.V. Egorysheva, T.I. Milenov, O.G. Ellert, G.V. Avdeev, P.M. Rafailov, N.N. Efimov, V.M. Novotortsev. *Solid State Sci.* **40**, 31 (2015).
- [9] H. Akamatsu, K. Tanaka, K. Fujita, S. Murai. *Phys. Rev. B* **74**, 012411 (2006).
- [10] K.L. Belov. *UFN*, **163**, 53 (1993). (in Russian).
- [11] W. Widanarto, M.R. Sahar, S.K. Ghoshal, R. Arifin, M.S. Rohani, K. Hamzah, M. Jandra. *Mater. Chem. Phys.* **138**, 174 (2013).
- [12] V.K. Tikhomirov, V.D. Rodríguez, A. Kuznetsov, D. Kirilenko, G. Van Tendeloo, V.V. Moshchalkov. *Opt. Express* **18**, 22032 (2010).
- [13] M.V. Shestakov, X.M. Chen, V. Kaydashev, W. Baeckelant, V.K. Tikhomirov, J. Vanacken, J. Hofkens, V.V. Moshchalkov. *Opt. Mater. Express* **4**, 1227 (2014).
- [14] V.D. Rodríguez, V.K. Tikhomirov, J.J. Velázquez, M.V. Shestakov, V.V. Moshchalkov. *Adv. Opt. Mater.* **1**, 747 (2013).
- [15] M. Dušek, V. Petříček. *Materials Structure in Chemistry, Biology, Phys. Technol.* **7**, 2, 85 (2020).
- [16] M. Aliahmad, N.N. Moghaddam. *Mater. Sci. Poland* **31**, 2, 264 (2013).
- [17] S. Sakurai, A. Namai, K. Hashimoto, S. Ohkoshi. *J. Am. Chem. Soc.* **131**, 18299 (2009).
- [18] J. Tuček, L. Machala, S. Ono, A. Namai, M. Yoshiakiyo, K. Imoto, H. Tokoro, S. Ohkoshi, R. Zboří. *Sci. Rep.* **5**, 15091 (2015).
- [19] R. Grau-Crespo, A.Y. Al-Baitai, I. Saadoune, & N.H. De Leeuw. *J. Phys.: Condens. Matter* **22**, 25, 255401 (2010).
- [20] H.L. Andersen, B.A. Frandsen, H.P. Gunnlaugsson, M.R.V. Jørgensen, S.J.L. Billinge, K.M.Ø. Jenseng, M. Christensen. *IUCrJ* **8**, 33 (2021).
- [21] U. Holzwarth, N. Gibson. *Nature Nanotechnol.* **6**, 534 (2011).
- [22] V. Mote, Y. Purushotham, B. Dole. *J. Theor. Appl. Phys.* **6**, 1 (2012).
- [23] T. Sekiya, N. Mochida, A. Ohtsuka, M. Tonokawa. *Nippon Seramikkusu Kyokai Rinbunshi* **97**, 12, 1435 (1989)
- [24] A.L. Geiler, V.G. Harris, C. Vittria, N.X. Sun. *J. Appl. Phys.* **99**, 08B316 (2006).

*Translated by E.Ilyinskaya*